

# Post Limiters and Simple Dirty-Cell Detection for Three-Dimensional, Unstructured, (Unlimited) Aerodynamic Simulations

K. Kitamura<sup>\*</sup>, T. Aogaki<sup>†</sup>, A. Inatomi<sup>‡</sup>, K. Fukumoto<sup>§</sup>, and T. Takahama<sup>\*\*</sup>  
Yokohama National University, Yokohama, Kanagawa 240-8501, Japan

and

A. Hashimoto<sup>††</sup>  
Japan Aerospace Exploration Agency (JAXA), Chofu, Tokyo 182-8522, Japan

The Post Limiter (simple *a posteriori* slope limiter) is an anti-slope-limiting mechanism to preserve nominal second order in space as much as possible. This technique has been demonstrated to increase resolutions of two-dimensional simulations up to four times in each dimension [Kitamura and Hashimoto, *Journal of Computational Physics*, Vol.341, 2017, pp.313-340]. This paper extends the Post Limiter to three dimensions (3D) with an emphasis on ‘dirty’ (=ill-shaped) cells, which arise in practical 3D unstructured grids over complex geometries. Gradient accuracy is known to significantly deteriorate on dirty cells, and a slope limiter needs to be applied. However, the original post limiter does not recognize dirty cells and deactivates a slope limiter. To address this issue, we propose a simple dirty-cell detection method and incorporate it into the Post Limiter. The 3D version of Post Limiter (referred to as ‘Post Limiter 3’) is successfully incorporated into FaST-Aerodynamic-Routines (FaSTAR), a 3D unstructured grid flow solver developed at Japan Aerospace Exploration Agency (JAXA). The Post Limiter 3 can handle general 3D unstructured grids. Numerical examples support its efficiency, accuracy, robustness, and applicability to a wide spectrum of aerodynamic problems of high engineering importance.

---

<sup>\*</sup> Associate Professor, Graduate School of Engineering, 79-5 Tokiwadai, Hodogaya-ku, AIAA Senior Member.

<sup>†</sup> Graduate Student, Graduate School of Engineering, 79-5 Tokiwadai, Hodogaya-ku, AIAA Student Member.

<sup>‡</sup> Graduate Student, Graduate School of Engineering, 79-5 Tokiwadai, Hodogaya-ku.

<sup>§</sup> Graduate Student, Graduate School of Engineering, 79-5 Tokiwadai, Hodogaya-ku.

<sup>\*\*</sup> Graduate Student, Graduate School of Engineering, 79-5 Tokiwadai, Hodogaya-ku.

<sup>††</sup> Associate Senior Researcher, Numerical Simulation Research Unit, Aeronautical Technology Directorate, 7-44-1 Jindaijihigashimachi, AIAA Senior Member.

## Nomenclature

$AR$	=	cell-aspect-ratio-like number
$C_D$	=	drag coefficient
$C_Y$	=	side force coefficient
$c_p$	=	specific heat at constant pressure
$E$	=	total energy per unit mass
$\mathbf{E}_k, \mathbf{F}_k$	=	inviscid and viscous flux vectors in $k$ -direction ( $k = 1, 2, 3$ , corresponding to $x, y, z$ , respectively)
$H$	=	total enthalpy
$M$	=	Mach number
$p$	=	pressure
$Pr$	=	Prandtl number, 0.71
$q$	=	primitive variable ( $\rho, u, v, w$ , or $p$ in 3D)
$\mathbf{Q}$	=	conservative variable vector
$\mathbf{r}$	=	position vector
$Re$	=	Reynolds number
$S$	=	area
$T$	=	temperature
$u_k$	=	velocity components in Cartesian coordinates
$V$	=	volume
$x_k$	=	Cartesian coordinates
$y^+$	=	non-dimensional wall distance
$\alpha$	=	angle of attack
$\phi$	=	( <i>a priori</i> ) limiter function, $\phi \in [0, 1]$
$\phi_G$	=	Gnoffo's auxiliary function, $\phi_G \in [0, 1]$
$\gamma$	=	specific heat ratio, 1.4
$\kappa$	=	thermal conductivity, $\kappa = \mu c_p / Pr$
$\mu$	=	molecular viscosity
$\rho$	=	density

$\theta_{face}$  = cell-orientation angle at cell-interface

### *Subscripts*

$i$  = cell  $i$

$i,j$  = interface between cells  $i$  and  $j$

$lim$  = limited value

$t$  = turbulent value

$unlim$  = unlimited value

## I. Introduction

COMPRESSIBLE computational fluid dynamics (CFD) has been actively used as a key analysis tool in aircraft and spacecraft designs [1-5]. Its reliability is particularly high in the range of Mach 0.1 – 0.7, in which numerical errors can be even one count ( $10^{-4}$  of drag coefficient,  $C_D$ ) order [6-9]. In aerodynamic simulations involving complex configurations, unstructured grids [9-13] are preferred to the structured counterparts from the following aspects: 1) The unstructured grids are easy to fit to complex geometries; 2) High grid-density can be locally realized in the region of flow-physics-rich; 3) Its reliability has been demonstrated by many prior works. For those unstructured grids, economical, spatially second-order accurate methods [14] are employed for efficiency [1-5].

Very recently, the authors have proposed a new strategy called “Post Limiter” [15] within the framework of second-order finite-volume-method (FVM). This Post Limiter tries to turn off the slope limiter as much as possible (even at shocks), and use un-limited gradients [16], in pursuit of truly second-order aerodynamic simulations. As a result, the Post Limiter attained a nearly four times resolution<sup>\*\*</sup> in one-dimension and 16 times in two dimensions, compared with a conventional method (i.e., without the Post Limiter). The Post Limiter has also been extended to unstructured, two-dimensional, triangular meshes [15], by taking account of cell-orientation angles [17].

Needless to say, in practical aerodynamic simulations, three-dimensional flows are computed around/in (typically complex) 3D geometries as mentioned above. Particularly near a 3D body wall, very thin cells are used to resolve boundary layers. These cells have very high aspect-ratios, and require special care because gradients computed for such cells can be erroneous [18]. Even worse, these thin cells are sometimes distorted, or skewed, with

---

<sup>\*\*</sup> The “four times resolution” stands for the improved resolution of the solution, which is equivalent with a solution on a finer grid composed of four times number of elements (cells).

nearly zero or even negative volumes – These ill-shaped cells are thus called “dirty-cells” in this work. On the dirty-cells, as a compromise between accuracy and robustness, it is practical to use only first-order reconstruction rather than employing troublesome gradients. This is usually realized by simply activating a slope limiter, such as minmod [19] there. The slope limiters were originally designed to deactivate reconstruction (= use of gradients) where abrupt changes of variables are observed and thus computations are “likely” to be destabilized. Slope limiters therefore can act also at dirty-cells, when the gradients there contain huge errors due to their highly-deformed cell geometries, or when computed cell-sizes change suddenly, e.g., at hanging nodes [9-13] (several limiters such as by Venkatakrishnan are functions of the cell-sizes [20]). This may be one of probable reasons why commercial and/or industrial codes can handle complex geometries (by sacrificing accuracy) without needing particular attentions paid by users (including beginners and even non-specialists). However, their know-hows are typically undisclosed.

Therefore, in this paper, we propose a simple, easy-to-use, and open “dirty-cell” detection method for an engineering purpose. Then it will be combined with the Post Limiter, and tested on selected numerical examples on 3D unstructured grids, for its practical use in a wide spectrum of aerodynamic simulations of high academic and industrial importance [21, 22].

The present paper is organized as follows. Section II will describe governing equations. Sections III-A and III-B will review the Post Limiters [15]. Then, Section III-C will propose a new, simple, dirty-cell detection method, and combine it with the Post Limiter as “Post Limiter 3.” The Post Limiter 3 will be tested on various aerodynamic examples in Sec. IV. Finally, Sec. V will summarize the current work. It should be noted that, in recent years, more sophisticated, higher-order methods such as discontinuous Galerkin [23], Flux-Reconstruction [24], spectral-volume [25], spectral-difference [25], or residual distribution [26, 27] have attracted CFD community, and may be used more widely in future. Nevertheless, many practitioners still desire a second-order FVM method for immediate use on 3D unstructured grids.

## II. Governing Equations

The governing equations are the compressible Euler or Navier-Stokes equations:

$$\frac{\partial \mathbf{Q}}{\partial t} + \frac{\partial \mathbf{E}_k}{\partial x_k} = \frac{\partial \mathbf{F}_k}{\partial x_k} \quad (1a)$$

$$\mathbf{Q} = \begin{bmatrix} \rho \\ \rho u_i \\ \rho E \end{bmatrix}, \quad \mathbf{E}_k = \begin{bmatrix} \rho u_k \\ \rho u_i u_k + p \delta_{ik} \\ \rho u_k H \end{bmatrix}, \quad \mathbf{F}_k = \begin{bmatrix} 0 \\ \tau_{ik} \\ u_j \tau_{jk} + \kappa \frac{\partial T}{\partial x_k} \end{bmatrix} \quad (1b)$$

$$\tau_{jk} = \mu \left( \frac{\partial u_j}{\partial x_k} + \frac{\partial u_k}{\partial x_j} \right) - \frac{2}{3} \mu \frac{\partial u_l}{\partial x_l} \delta_{jk} \quad (1c)$$

where  $\rho$  is density,  $u_k$  velocity components in Cartesian coordinates ( $k = 1, 2, 3$  correspond to  $u, v, w$ , respectively),  $E$  is total energy per unit mass,  $p$  is pressure,  $H$  is total enthalpy ( $H = E + (p/\rho)$ ), and  $T$  is temperature. The working gas is air approximated by the calorically perfect gas model with the specific heat ratio  $\gamma=1.4$ . The Prandtl number is  $Pr=0.71$ . The molecular viscosity  $\mu$ , calculated by the Sutherland's formula, and thermal conductivity  $\kappa$  are related as  $\kappa=c_p\mu/Pr$  where  $c_p$  is the specific heat at constant pressure; In the Euler cases,  $\mu$  and  $\kappa$  are merely turned off ( $\mu=\kappa=0$ ). In the turbulence calculations, molecular viscosity  $\mu$  is replaced by  $(\mu+\mu_t)$ , where  $\mu_t$  is turbulence viscosity; likewise,  $\kappa$  is replaced by  $(\kappa+c_p\mu_t/Pr_t)$ , and  $Pr_t$  is turbulent Prandtl number, 0.90.

Equation (1) is discretized and expressed in FVM form as follows:

$$\frac{V_i}{\Delta t} \Delta \mathbf{Q}_i + \sum_j (\mathbf{E}_{i,j} - \mathbf{F}_{i,j}) S_{i,j} = 0 \quad (2)$$

where  $V_i$  stands for the volume of the cell  $i$ ,  $\Delta t$  is the time step,  $\Delta \mathbf{Q}_i$  is change of conservative variables in time,  $\mathbf{E}_{i,j}$  and  $\mathbf{F}_{i,j}$  are the inviscid (Euler) and viscous fluxes through the cell-interface  $S_{i,j}$  (which separates the cell  $i$  and its neighbor cell  $j$ ), respectively (see Fig. 1 for a cell geometric schematic).

### III. Post Limiters

#### A. Post Limiter 1 (for Smooth Structured Grids)

The Post Limiter was designed for use in a second-order finite-volume method on unstructured grids. In the second-order method, a candidate value at a cell-interface is either the second-order extrapolated value  $q^{unlim}$  or its limited, first-order value  $q^{lim}$ . Remembering the fact that those values are obtained almost at one time (within the

same “do” loop in the numerical code), the Post Limiter can choose the cell-interfacial value from these two, or even blend them – This is the core concept of the Post Limiter [15] (Fig. 2). To be more specific, the unlimited value  $q^{unlim}$  is adopted when i) positivity and ii) DMP (Discrete Maximum Principle) are satisfied for density and pressure, following [28], and also when iii) the pressure ratio between the current and the neighbor cells is nearly unity (in the case of pressure ratio between one and two,  $q^{unlim}$  and  $q^{lim}$  are blended by a smooth function  $\phi_G$  by Gnoffo [29]). The whole procedure is summarized in the form of a flow chart in Fig. 3a. This method will be called “Post Limiter 1” for convenience, and its detailed explanations and performances are found in [15].

### B. Post Limiter 2 (for 2D Triangular Unstructured Grids)

The Post Limiter 1 was designed for use in 1D, and it actually performed very well on 1D or structured, smooth 2D grids (in which one-dimensional treatments are straightforward), i.e., four times resolution in 1D, and almost 16 times resolution in 2D with improved convergence. On the contrary, on unstructured 2D grids such as triangular meshes, a cell-center is not usually located in the normal direction of its cell-interface, and hence, multi-dimensional geometrical considerations are required. Specifically, the Gnoffo’s function (now the original value is denoted by  $\phi_G$ ) needs the following slight modification to the final value  $\phi_G'$  (“Post Limiter 2”).

$$\phi_G' = \min(\phi_G, \phi_{face}) \quad (3a)$$

$$\phi_{face} = 0.25(\cos(\theta_{face}) + |\cos(\theta_{face})|)^2 \quad (3b)$$

where  $\theta_{face}$  stands for a “cell orientation-angle” borrowed from [17], as defined in Fig. 1. This is given by an inner product of  $(\mathbf{r}_{ij} - \mathbf{r}_i)$  and  $(\mathbf{r}_j - \mathbf{r}_{ij})$ , where  $\mathbf{r}_{ij}$ ,  $\mathbf{r}_i$ , and  $\mathbf{r}_j$  are the position vectors of the cell-interfacial center  $ij$ , the cell-center  $i$ , and the cell-center  $j$ , respectively. If these three points are aligned in the same line (as in 1D or Cartesian meshes),  $\theta_{face}$  is zero and  $\phi_{face}$  is unity. Thus, the method reduces to unmodified, Post Limiter 1. On the other hand, if  $\theta_{face}$  exceeds 90 degrees,  $\phi_{face} = 0$  and the Post Limiter does not act (i.e., the slope limiter is more likely activated). As for  $\theta_{face}$  between 0 and 90 degrees,  $\phi_{face}$  is smoothly connected by Eq. (3b). Therefore, the modification here is still simple and local.

### C. Simple Dirty-Cell Detection and Post Limiter 3 (for General 3D Unstructured Grids)

As stated above, the so-called dirty-cells (i.e., cells of poor quality) can appear in 3D [8]. This is because, in contrast with 1D or 2D, the following situations can arise.

- A face is composed of nodes (four or more) that are *not on the same plane* (Fig. 4a).
- A (hexahedral or prism) cell is composed of its *upper face* and *lower face* that are partly *flipped over* in their relative positioning (Fig. 4b).
- A cell is composed of *edges intersecting faces* (Fig. 4c).

In those or other many similar cases, the calculated cell-volume  $V_i$  will be very small, or even negative, leading to divergence of flow computations. There exists an individual evaluation method for every aspect of cell qualities (e.g., using edge lengths or vectors, diagonal lengths or vectors, angles, Jacobians) as introduced in Ref. [30] for over 100 pages. It is, however, cumbersome and unpractical to incorporate all those evaluation methods into a flow computation code, and those quantities are not necessarily available in an unstructured flow simulation code. In addition, those dirty-cells are observed typically near a body wall. Thus, we propose a simpler detection method for potential dirty-cells of relatively high risk of computational blow-up:

$$AR \cong \max \left( \frac{V_i^{2/3}}{S_{i,j}}, \frac{V_j^{2/3}}{S_{i,j}}, \frac{S_{i,j}}{V_i^{2/3}}, \frac{S_{i,j}}{V_j^{2/3}} \right) < 4 \quad (4)^{\S\S}$$

This value can be interpreted as follows: i) the cell length normal to the interface is approximated by  $b \equiv V_{i \text{ or } j} / S_{i,j}$ , where  $V_{i \text{ or } j}$  is the cell volume and  $S_{i,j}$  is the interface area; ii) the cell length tangential to the interface, on the other hand, is represented by  $a \equiv V_i^{1/3}$ ; iii) then,  $AR \equiv b/a$ , and its inverse are obtained for both  $i$  and  $j$  cells; iv) finally, its maximum value is adopted for evaluation. If this aspect-ratio-like number ( $AR$ )<sup>\*\*\*</sup> exceeds the prescribed value, the Post Limiter will be turned off, that is, the slope limiter can be activated. This criterion has the following three advantages.

1) It is clearly based on our concept that we will not use the Post Limiter on a cell with high aspect-ratio. The Post Limiter is inherently suitable to cells with good quality [15], and hence, the present criterion matches well with this concept.

2) The  $AR$  value of the cube is unity. Other typical cell geometries and the corresponding  $AR$  values are listed in Table 1. As seen, this number is a good indicator as to how the cell-of-interest is closer to the cube geometry;

---

<sup>\S\S</sup> It may be more precise to use the common right and left cells for reconstruction and also for defining  $AR$  in Eq.(4). However, since many solvers used today are already established and their code structures differ from one to another, we decided to offer those users/practitioners a simple method which is applicable to any of those codes.

<sup>\S\S\S</sup> Remember that the wing aspect-ratio is given by  $AR=b^2/S$ , where  $b$  is the span length and  $S$  is the wing area.

otherwise, the Post Limiter will be deactivated and the slope limiter will likely to be used. What is more, this value is away from unity also where the cell sizes change abruptly.

3) The Eq. (4) needs little additional information. The cell volumes  $V_i$ ,  $V_j$  and the interfacial area  $S_{i,j}$  used in this equation are necessary components of the solver, as evident in Eq. (2). Thus, at the time of the limiter computation, they are already known or readily available on an unstructured grid solver.

According to our preliminary numerical tests, the threshold value is determined as four<sup>†††</sup>. Many cells near the wall will have  $AR$  exceeding this value, and then the Post Limiter will be turned off (i.e., a limiter can be used) there. This results in possible accuracy degeneracy. This is, however, not a problem because calculated gradients along surfaces with high curvature (such as a sphere surface) are known to potentially contain significant errors due to huge cell-aspect-ratio [18]. Then, a slope limiter is useful to suppress those numerical errors by not adopting the gradient.

From the strengths mentioned above, the aspect-ratio-like number ( $AR$ ) will be added to the determinant criteria of Post Limiter 2. Specifically, if the cell-interface does not satisfy Eq. (4), either of cells of its both sides  $i$  or  $j$  (Fig. 1) can be of a poor quality, and then  $\phi_G = 0$  is forced, that is, the limited, first-order  $q^{lim}$  is adopted<sup>†††</sup>. This version of the Post Limiter is coined as “Post Limiter 3” hereafter. Figure 5 shows its flow chart, and Table 2 summarizes the Post Limiters 1 through 3. The Post Limiter 3 has been successfully incorporated into FaST-Aerodynamic-Routines (FaSTAR) [9], a 3D unstructured grid solver developed at JAXA. FaSTAR checks whether the given mesh contains no cells of negative volume before flow computations; but other solvers having no such procedure will require this negative volume check to be included in the Post Limiter 3.

#### IV. Numerical Examples

In the following numerical examples, Post-Limiter-3-incorporated FaSTAR is used as a flow solver. Unless otherwise stated, Green-Gauss method [31] is used for gradient computation (spatial reconstruction), and this

---

<sup>†††</sup> If we chose 10, then, it worked in some cases but not in others; 100 led to computational divergence in many cases; 1 means Post Limiter works only on cubes (hex), which is not our intention. Therefore, 4 is one of the currently-available best choices.

<sup>†††</sup> In fact, this additional part for Post Limiter 3 and that for Post Limiter 2 are both on the mesh geometry, and thus can be combined and computed only once ahead of whole the flow computation for efficient implementation. This is quite effective, unless the moving and/or deforming grid is used – these will also be coupled with the present method in the future, and thus, the present form in Fig. 5 (i.e., the cell geometrical property is computed at each time step) will be kept in this work.



gradient is used to obtain a cell-interfacial value  $q_{i,j}$  from a cell-center value  $q_i$ ; then SLAU [32] is used to compute numerical flux across the interface; Lower-Upper Symmetric Gauss-Seidel [33] is used for time integration; turbulence viscosity  $\mu_t$  is computed by Spalart-Allmaras model [34] without a tripping term (sometimes denoted as SA-noft2 model) [35] or Delayed Detached-Eddy Simulation [36] in turbulent computations. The slope limiter will be explained in each case. In most of the test cases (except for IV.B), HexaGrid [9] developed at JAXA is used as the grid generation tool: It automatically generates unstructured grids based on hexahedra Cartesian grids (along with tetrahedra, pyramids, and prisms).

In IV-A, a subsonic flow around a sphere is solved, and the solutions and convergence rates by different limiters and Post Limiter 3 are compared. In IV-B, a subsonic flow around two-dimensional airfoil is treated, in which effects of grid density is discussed. In IV-C and IV-D, three-dimensional flows around spacecraft and aircraft are solved, respectively, with or without Post Limiter 3. Additional examples involving shockwaves will be found in Appendix.

#### **A. Subsonic, Viscous Flow over Sphere ( $M = 0.1$ , $Re = 118$ )**

This test case is a subsonic flow of Mach 0.1, Reynolds number 118, past a sphere. This example has been often used as a benchmark for Navier-Stokes Equations, since both a converged solution [37] and the reference experimental results [38] of steady, twin-vortex flow are available in literature. In addition, since no shock waves are expected in this flow, it is favorable for the slope limiter not to be activated. Here the minmod limiter is selected as a slope limiter, and combined with Post Limiter 3. Since the Reynolds number is sufficiently small, no turbulence model is employed.

The computational grid, composed primarily of hexahedra (along with prisms, pyramids, and tetrahedra), is generated around the sphere (only for its half-domain,  $y \leq 0$ ) using HexaGrid [9] (Fig. 6a, colored with  $AR$  for  $1 \leq AR \leq 4$ ). The sphere diameter is 1, the minimum cell width is  $1.e-3$  (maximum  $AR = 11.9$ ) near the wall, and the outer boundary of the computational domain is a cube having 20 side length (the sphere is located almost in the cube center), filled with hexahedra (cube cells,  $AR = 1$ ) and the other cell geometries ( $AR \approx 3$ ). The total number of cells is 396,010.

The (steady flow) computations were conducted with  $CFL=1,000$  (10,000 time steps). Figure 6b shows density residuals, which demonstrate the superiority of Post Limiter 3 in convergence (nearly two orders of residual reduction). This is because, similarly to structured grid cases [15], the minmod limiter is not used at unnecessary

places. In Figs. 6c and 6d, visualized computed flow fields (pressure and wake velocity-vectors) are displayed. These figures demonstrate that the computed solution (Fig. 6c) is unaffected by Post Limiter 3, producing wake twin-vortex as in the case without Post Limiter 3 (Fig. 6d) or in reference [38]. In addition, either with or without Post Limiter 3, the computed drag coefficient was  $C_D = 1.02$ , which almost agrees with the value by Schlichting ( $C_D \approx 1.0$  at  $Re \approx 120$ ) [39]. Moreover, Fig. 6e displays pressure differences between the cases with and without Post Limiter 3. It is confirmed from this figure that only slight differences ( $C_p \approx 0.01$ ; its infinity-norm being 0.04) exist where cubic cells ( $AR = 1$ ) are *not* used. What is more, though not shown, the results using Post Limiter 1 and Post Limiter 2 also matched with the Post Limiter 3 results.

### B. Two-Dimensional Airfoil ( $M = 0.2$ , $Re = 23,000$ , $\alpha = 6^\circ$ )

This example is a low Reynolds number flow ( $M_\infty=0.2$ ,  $Re=23,000$ , and an angle-of-attack  $\alpha=6^\circ$ ) past the owl-like airfoil. This flow is laminar, involving a leading-edge separation and a trailing-edge reattachment (that are both difficult to be captured by flow simulations) as reported in [40]. Here a van\_Leer-type Hishida limiter [Hishida (vL)] [41] is employed, combined with or without Post Limiter 3. The gradient is calculated by Green-Gauss-weighted Least-Squares (GLSQ) [31], numerical flux is computed by SLAU [32], and no turbulence model is employed.

A two-dimensional, C-type, structured grid is used as shown in Fig. 7a (colored for  $1 \leq AR \leq 50$ ); 614 cells are used in the circumferential direction, whereas 100 cells in the wall/wake-normal direction in Baseline grid (likewise, 306x50 cells in Coarse grid); The minimum spacing achieves  $0.01/Re^{0.5}=6.59 \times 10^{-5}$  (maximum  $AR = 930$ ) near the wall, where the chord length is unity, and the far field boundary is located at 50 times the chord length away. The airfoil geometry used here corresponds to the 40% spanwise wing section from the wing-root [42]. The unsteady computations were conducted long enough to extract time-averaged results for 15 periods.

The results are shown in Fig. 7b-7d: On Coarse grid, without Post Limiter 3, the leading-edge separation is observed, while the trailing-edge reattachment is not captured (Fig. 7b); with Post Limiter 3, on the other hand, this trailing-edge reattachment is successfully resolved (Fig. 7c) as well as on Baseline grid (without Post Limiter 3) (Fig. 7d). In other words, the conventional method (i.e. without Post Limiter 3) requires Baseline grid (having 2x2 times resolution compared with Coarse grid) to reproduce the reattachment, whereas Coarse grid is enough for the Post Limiter 3.

### C. Three-Dimensional Slender Body at High Angle-of-Attack ( $M = 0.086$ , $Re = 6 \times 10^5$ , $\alpha = 50^\circ$ )

This is a more practical case of a three-dimensional, slender body at a high angle-of-attack ( $\alpha = 50^\circ$ ). This configuration consists of hemisphere-cone-square\_prism [i.e., its cross-sectional shape gradually changes from the circle (near the nose) to the (filleted) square (near the base)], and considered as one of candidates as a new reusable rocket at JAXA (for details, see Refs. [43, 44]). Since the uniform flow Mach number is small ( $M = 0.086$ ), the all-speed numerical flux SLAU is used along with preconditioned LU-SGS [45, 46] for time integration. The gradients are computed by GLSQ. The Reynolds number based on the body length is  $Re = 6 \times 10^5$ , and hence, we employ SA-nof2 model to compute turbulent viscosity.

The computational grid is composed of 1.75 million cells (of hexahedra, prisms, pyramids, and tetrahedra), containing a dense region at the leeward side in which vortices are expected to develop at high attack angles (Fig. 8; colored for  $1 \leq AR \leq 4$ ; maximum  $AR = 81.3$ ). Figure 8 shows only the slender body vicinity, but the outer boundary is 25 times the body length away from the body. The minimum cell width is  $y^+ = 0.78$ . It is seen that cells of mild  $AR$  ( $1 < AR < 4$ ) appears where cell sizes change from smaller cubes to larger ones, and those of higher  $AR$  ( $AR \geq 4$ ) are located near the body wall. Now the minmod limiter is used as a slope (*a priori*) limiter, and examine the effects of Post Limiter 3. Since the flow is subsonic, the case *without* a limiter will also be conducted for reference.

Figure 9 shows computed flow results: pressure and axial vorticity, along with an absolute value of a side force coefficient  $|C_Y|$  (as an indicator of asymmetry). At such a high angle, asymmetry flow is known to be observed around the slender body [47, 48]. In Figs. 9a and 9b (minmod-only), however, the flow is almost symmetry, and the  $|C_Y|$  is very small ( $|C_Y| = 0.052$ ). In contrast, with the Post Limiter 3, clear asymmetry emerges and the side force  $|C_Y| = 0.312$  is produced (Figs. 9c and 9d). In addition, without the minmod limiter (Figs. 9e and 9f), the asymmetry is more notable, with the enhanced side force  $|C_Y| = 0.812$ . Therefore, thanks to the Post Limiter 3, the minmod limiter has been deactivated at unnecessary places ( $AR < 4$ ), even on a three-dimensional unstructured grid at low-speed flow. This has resulted in the closer solution to the asymmetry flow obtained by the case without the minmod limiter. The same trend has been observed when the body has 45 deg. of rotation angle (not shown) as in [43].

In fact, as in this example, if it is already known that the computation is possible without the limiter, it is of course recommended to turn off the limiter in advance. In most of practical flow simulations, however, low speed and high speed flows coexist, and the high speed flow regions call for the limiter to stabilize shocks. Since these high speed regions are *unidentified* before the computation, the limiter is needed for the entire computational

*domain*. For this reason, the Post Limiter 3 is very helpful for both the flow resolution and the computational robustness.

#### **D. Low Speed Buffet Flow around Three-Dimensional Aircraft ( $M = 0.25$ , $Re = 1.16 \times 10^7$ , $\alpha = 18^\circ$ )**

Another practical simulation is conducted here: three-dimensional, unsteady, turbulent flow computation around aircraft [49]. The aircraft configuration and its surrounding computational grid (22.8M cells of hexahedra, prisms, pyramids, and tetrahedra: *designated as Baseline grid*) are shown in Fig. 10a. Because of the complex geometry such as high curvature and wing/body junctions, this grid contains many dirty-cells (Fig. 4) near the body wall (*colored for  $1 \leq AR \leq 4$ ; maximum  $AR = 361.6$* ). This is not an untypical case, which usually needs a slope limiter to stabilize the computation there.

The Hishida (vL) slope limiter is used with Green-Gauss for slope computation, SLAU numerical flux, DDES turbulence model, and LU-SGS along with dual-time-stepping (five inner-iterations) for time integration. The unsteady flow computations were conducted with  $\Delta t = 2.2e-5$  [s] ( $CFL \approx 10,000$ ) until 27,000 timesteps. Various versions of Post Limiters were coupled, and the results are summarized in Table 3: Post Limiter 1 and Post Limiter 2 cases diverged, obviously because of dirty-cells that destabilized the computations, as evidenced by the case without limiter; on the other hand, Post Limiter 3 was able to compute this problem, as well as the case without Post Limiter [i.e., Hishida (vL) slope limiter only]. Then, power spectral density (divided by specific ratio and square of freestream pressure) profiles over the last 9,000 steps at a point in the main wing wake almost agree between those two cases (Fig. 10b). *Figures 10c and 10d compare pressure profiles on the top (leeward) surface of the aircraft. They almost agree with each other, except for the wing root region. We also plotted the pressure distributions at 28.3% spanwise position of the main wing in Fig. 10e, and confirmed good agreement among the two numerical solutions and the experimental data from [49].* In other words, it has been demonstrated that Post Limiter 3 properly detected dirty-cells and triggered the slope limiter at necessary places.

Finally, we have conducted the same set of computations on *Coarse* grid (15.4M cells) (Fig. 11). The case *without* the Post Limiter 3 [i.e., Hishida (vL)-only, Coarse] exhibit variations from the Baseline grid solution in surface pressure contours (Fig. 11a), and in pressure distribution at 28.3% spanwise position (Fig. 11c), especially near the leading-edge (Fig. 11d). On the contrary, the case *with* the Post Limiter 3 [i.e., Hishida (vL)+Post Limiter 3, Coarse] showed little sensitivity against the mesh density (Figs. 10d, 11b-11d). That is to say, the Post Limiter 3 solutions almost achieved the grid convergence.

## V. Conclusions

The “Post Limiter (simple *a posteriori* slope limiter),” which tries to keep spatially second order as much as possible, has been successfully extended to three-dimensional (3D) unstructured grids. This was achieved by proposing a new, simple detection method for “dirty” (= ill-shaped) cells, by taking account of only ‘cell-aspect-ratio-like number’ introduced in this work. Then the 3D-extended version of Post Limiter (referred to as ‘Post Limiter 3’) was successfully incorporated into “FaSTAR,” a 3D unstructured grid flow solver developed at Japan Aerospace Exploration Agency (JAXA). The Post Limiter 3 can handle general 3D unstructured grids with satisfactory efficiency, accuracy, and robustness, as demonstrated by numerical examples in a wide spectrum of aerodynamic problems: subsonic flow over a sphere, low Reynolds flow over an airfoil, slender body at high angle-of-attack, and low speed buffet around an aircraft.

The future work will involve applications to various fluids other than the perfect-gas-modeled air, i.e., multiphase flow, supercritical flow, and magneto-hydro-dynamics (MHD).

## Acknowledgments

In the flow computations presented here, 3D unstructured grid flow solver “FaSTAR” developed at JAXA has been used. In several numerical tests, a grid generator “HexaGrid” by JAXA and JAXA’s Super Computer 2 (JSS2) also have been used. Mr. Kenji Hayashi at Ryoyu Systems, Inc. (Japan), extracted and visualized dirty cells. Dr. Hiroaki Nishikawa at National Institute of Aerospace (USA) kindly revised the present manuscript to improve its quality. Mr. Suguru Ogawa, Yokohama National University, Japan, helped us with visualizing the *AR* for the grid around the owl-like airfoil. We are grateful to all their cooperation.

## Appendix: Numerical Examples with Shock Waves

The following subsections A and B will deal with transonic shock/vortex interaction and supersonic flows, respectively. These two cases will attempt to extend the Post Limiter 3 to transonic and supersonic flows, although the Post Limiter was originally proposed to improve flow solution resolution and convergence at subsonic speeds.

### A. Shock/Vortex Interaction on Triangular Mesh (M = 1.1, Inviscid)

Now that we have confirmed desired performance of Post Limiter 3 on 3D unstructured grids including dirty-cells at subsonic speeds, let us try to apply it to supersonic flows involving shocks. The test case here is unsteady shock/vortex interaction by Jiang-Shu [50]. The computational domain and conditions are the same as in [15]: The computational domain is  $[0, 2] \times [0, 1]$  divided by 249,756 triangular cells (Figs. A.1a and A.1b, a coarser grid of 15,676 is displayed for visualization purpose;  $6.6 \leq AR \leq 10.2$ ), automatically generated by the commercial software Pointwise<sup>®</sup> developed by Pointwise, Inc. The inflow condition is imposed at the left boundary, the outflow condition at the right boundary (with pressure fixed), and the slip condition is applied to the top and bottom boundaries. The initial conditions are as follows:

- 1) A Mach 1.1 shockwave is given at  $x = 0.5$ . Its left side is:

$$(\rho, u, v, p)_L = (1, \sqrt{\gamma}, 0, 1) \text{ for } x \leq 0.5$$

- 2) The right side condition is then provided to satisfy the Rankine-Hugoniot condition.
- 3) Furthermore, the following vortex centered at  $(x_c, y_c) = (0.25, 0.5)$  is superimposed as perturbations to the initial flow.

$$\left. \begin{aligned} \Delta u &= \varepsilon \tau \exp(\alpha(1-\tau^2)) \cdot \frac{\Delta y}{r} \\ \Delta v &= -\varepsilon \tau \exp(\alpha(1-\tau^2)) \cdot \frac{\Delta x}{r} \\ \Delta T &= -\frac{(\gamma-1)\varepsilon^2 \exp(2\alpha(1-\tau^2))}{4\alpha\gamma}; \quad \Delta p = (\Delta T + 1)^{\frac{\gamma}{\gamma-1}} - 1; \quad \Delta \rho = (\Delta p + 1)^{\frac{1}{\gamma}} - 1 \end{aligned} \right\} \quad (5a)$$

where

$$\left. \begin{aligned} \tau &= r/r_c, \quad r = \sqrt{(\Delta x)^2 + (\Delta y)^2} \\ \Delta x &= x - x_c, \quad \Delta y = y - y_c \\ \varepsilon &= 0.3, \quad r_c = 0.05, \quad \alpha = 0.204 \end{aligned} \right\} \quad (5b)$$

Note that the gridlines are *not* intentionally aligned to the initial shock, and thus, the shock in this test crosses the cells with many possible angles, as in practical flow computations. The SLAU2 [51] (which is an enhanced version of SLAU for super- and hypersonic flows) is used to compute numerical flux. The least-squares method is used for spatial reconstruction, because it is known to be more appropriate to triangles [31]. The slope limiter is minmod. The time step is prescribed at  $\Delta t = 2.e-4$  (CFL $\approx$ 0.6), and the computation is conducted to 3,000 steps ( $t = 0.6$ ) by standard two-stage, second-order Runge-Kutta method.

The computed flowfields of “minmod-only,” “minmod + Post Limiter 2,” and “minmod + Post Limiter 3” cases are compared by extruded 3D pressure contours (color and azimuth) in Figs. A.1c – A.1e, as in [15, 52]. It is already reported in [15] that the Post Limiter 1 cannot handle this problem on triangular grids. The Post Limiter 2 and Post Limiter 3, in contrast, are able to compute this test with slightly fewer wiggles (Figs. A.1d, A.1e) than the minmod-only case (Fig. A.1c). This result is reasonable, considering the fact that the minimum  $AR$  is 6.6 in this case. In other words, Post Limiter 3 is able to conduct the shock-involved flow simulation on the triangular grid without raising spurious numerical wiggles.

### B. Supersonic Parachute ( $M = 2.0$ , $Re = 2 \times 10^6$ )

Finally, the Post Limiter 3 is applied to a supersonic flow around a parachute. This supersonic parachute is a so-called “Disk-Gap-Band” type [53, 54], comprised of spheroid (Disk) and cylinder (Band) parts separated by Gap (Fig. B.1; details can be found in [55]). The freestream Mach number is 2.0, and the Reynolds number based on Disk diameter of 0.07 [m] is  $2 \times 10^6$  [55]. Deformation of the parachute is not taken into account, as in the corresponding wind-tunnel experiment employing a rigid body [54]. Only the half-domain is considered due to flow symmetry.

Figures B.2a and B.2b show Coarse (2.8M cells) and Fine (10.5M cells) grids, respectively, both composed of hexahedra, prisms, pyramids, and tetrahedra. The minimum spacing of  $1.83 \times 10^{-5}$  [m] ( $y^+ \approx 0.6$ ) is common in the wall-normal direction, while in the wall-tangential direction it is  $5.86 \times 10^{-4}$  [m] for Coarse grid and  $2.93 \times 10^{-4}$  [m] for Fine grid: this difference leads to different cell sizes not only near the wall but also of the Cartesian (hexahedra) portion away from the wall. Figure B.2c shows the  $AR$  distribution for the Coarse grid (colored for  $1 \leq AR \leq 4$ ), and Fig. B.2d displays its close-up view around the Band vicinity. As seen, the  $AR$  is unity for the cube cells, whereas it is higher near the wall (prisms:  $AR \leq 6.7$ ) and other cell geometries (pyramids and tetrahedra:  $AR \approx 3$ ).

The Venkatakrisnan [20] slope limiter (standalone, with Post Limiter 2, or with Post Limiter 3) is used along with SLAU for numerical flux, GLSQ for slope computation, SA-noft2 for turbulent viscosity, and LU-SGS with dual-time-stepping (fixed time interval of  $\Delta t = 5.25e-8$  [s] with five inner-iterations, corresponding to  $CFL \approx 19$  on Coarse grid;  $CFL \approx 44$  on Fine grid) for time integration. The selected results are shown in Fig. B.3. The Post Limiter 2 computation on Coarse grid blew up in the wake of the parachute (indicated by a red cross in Fig. B.3a), where expanded flow passes through tetrahedra cells around which cell sizes abruptly change. The Post Limiter 3 (on Coarse grid), on the other hand, successfully continued to compute this flow (Fig. B.3b). The resultant drag

coefficient was  $C_D = 0.875$  (time-averaged between 15,000 – 20,000 timesteps), which is close to the experimentally measured value  $C_D \approx 0.88$  [54]. Similar values were also obtained by Venkatakrishnan-limiter-only, both on Coarse grid ( $C_D = 0.874$ ) and Fine grid ( $C_D = 0.875$ ). However, after 5,000 timesteps, the case of Venkatakrishnan-limiter-only on Coarse grid exhibit an order of higher density residual than in Venkatakrishnan + Post Limiter 3 case or the case of Venkatakrishnan-only on Fine grid (Fig. B.4). In view of these results, Venkatakrishnan + Post Limiter 3 on Coarse grid, or Venkatakrishnan-only on Fine grid, seemed to have captured the wake structure (of the Reynolds-Averaged-Navier-Stokes equation resolution, at least) more accurately, whereas Venkatakrishnan-only on Coarse grid appeared to be insufficient in its resolution, and hence, led to numerical oscillations in time. Therefore, the solution with Post Limiter 3 is again superior to the one without it, or with Post Limiter 2, in the flow resolution and robustness.

#### References

- [1] Abdol-Hamid, K.S. and Ghaffari, F., “Ares I Vehicle Computed Turbulent Ascent Aerodynamic Data Development and Analysis,” *J. Spacecraft and Rockets*, Vol. 49, No.4 (2012), pp.596-608.
- [2] Schauerhamer, D.G., Zarchi, K.A., Kleb, W.L., Carlson, J.-R., and Edquist, K.T., “Supersonic Retropropulsion Computational Fluid Dynamics Validation with Langley 4×4 Foot Test Data,” *Journal of Spacecraft and Rockets*, Vol. 51, No. 3 (2014), pp. 693-714.
- [3] Kitamura, K., Nonaka, S., Kuzuu, K., Aono, J., Fujimoto, K., and Shima, E., “Numerical and Experimental Investigations of Epsilon Launch Vehicle Aerodynamics at Mach 1.5,” *J. Spacecraft and Rockets*, Vol.50 (2013), pp.896-916.
- [4] Gnoffo, P., Buck, G., Moss, J., Nielsen, E., Berger, K., Jones, W.T. and Rubavsky, R., “Aerothermodynamic Analyses of Towed Ballutes,” AIAA Paper 2006-3771, 2006.
- [5] Catalano, P., Marini, M., Nicoli, A. and Pizzicaroli, A., “CFD Contribution to the Aerodynamic Data Set of the Vega Launcher,” *J. Spacecraft and Rockets*, Vol. 44 (2007), pp.42-51.
- [6] Rumsey, C.L. and Slotnick, J.P., “Overview and Summary of the Second AIAA High-Lift Prediction Workshop,” *Journal of Aircraft*, Vol. 52, Special Section on Second High Lift Prediction Workshop (2015), pp. 1006-1025.
- [7] Vassberg, J.C., Tinoco, E.N., Mani, M., Rider, B., Zickuhr, T., Levy, D.W., Brodersen, O.P., Eisfeld, B., Crippa, S., Wahls, R.A., Morrison, J.H., Mavriplis, D.J. and Murayama, M., “Summary of the Fourth AIAA Computational Fluid Dynamics Drag Prediction Workshop,” *Journal of Aircraft*, Vol. 51, No. 4 (2014), pp. 1070-1089.
- [8] Mavriplis, D.J., Vassberg, J.C., Tinoco, E.N., Mani, M., Brodersen, O.P., Eisfeld, B., Wahls, R.A., Morrison, J.H., Zickuhr, T., Levy, D., and Murayama, M., “Grid Quality and Resolution Issues from the Drag Prediction Workshop



Series,” *Journal of Aircraft*, Vol. 46, No. 3 (2009), pp. 935-950.

[9] Hashimoto, A., Murakami, K., Aoyama, T., Yamamoto, K., Murayama, M. and Lahur, P. R., “Drag Prediction on NASA Common Research Model Using Automatic Hexahedra Grid-Generation Method,” *Journal of Aircraft*, Vol.51 (2014), pp. 1172-1182.

[10] Luo, H., Spiegel, S., and Löhner, R., “Hybrid Grid Generation Method for Complex Geometries,” *AIAA Journal*, Vol.48 (2010), pp. 2639-2647.

[11] Kidron, Y., Mor-Yossef, Y., and Levy, Y., “Robust Cartesian Grid Flow Solver for High-Reynolds-Number Turbulent Flow Simulations,” *AIAA Journal*, Vol.48 (2010), pp. 1130-1140.

[12] Ochi, A., Ibrahim, M.K., and Nakamura, Y., “Computational Fluid Dynamics Validation Study of Wake-Capturing Capability for a Flat-Plate Wake,” *Journal of Aircraft*, Vol. 47 (2010), pp. 441-449.

[13] Wang, Z.J., and Chen, R.F., “Anisotropic Solution-Adaptive Viscous Cartesian Grid Method for Turbulent Flow Simulation,” *AIAA Journal*, Vol. 40 (2002), pp.1969-1978.

[14] Van Leer, B., “Towards the Ultimate Conservative Difference Scheme. V. A Second-Order Sequel to Godunov’s Method,” *Journal of Computational Physics*, Vol. 32 (1979), pp.101-136.

[15] Kitamura, K. and Hashimoto, A., “Simple *a posteriori* slope limiter (Post Limiter) for high resolution and efficient flow computations,” *Journal of Computational Physics*, Vol. 341 (2017), pp.313-340.

[16] Suresh, A. and Huynh, H.T., “Accurate Monotonicity-Preserving Schemes with Runge-Kutta Time Stepping,” *Journal of Computational Physics*, Vol. 136 (1997), pp.83-99.

[17] Kitamura, K. and Hashimoto, A., “Reduced dissipation AUSM-family fluxes: HR-SLAU2 and HR-AUSM<sup>+</sup>-up for high resolution unsteady flow simulations,” *Computers and Fluids*, Vol. 126 (2016), pp. 41–57.

[18] Shima, E., Kitamura, K., and Haga, T., “Green-Gauss/ Weighted-Least-Squares Hybrid Gradient Reconstruction for Arbitrary Polyhedra Unstructured Grids,” *AIAA Journal*, Vol.51 (2013), pp.2740-2747.

[19] Roe, P.L., “Characteristic-based schemes for the Euler equations,” *Annual Review of Fluid Mechanics*, Vol.18 (1986), pp.337–365.

[20] Venkatakrishnan, V., “Convergence to Steady State Solutions of the Euler Equations on Unstructured Grids with Limiters,” *Journal of Computational Physics*, Vol. 118 (1995), pp.120-130.

[21] Kanamori, M., Takahashi, T., Naka, Y., Makino, Y., Takahashi, H., and Ishikawa, H., “Numerical Evaluation of Effect of Atmospheric Turbulence on Sonic Boom Observed in D-SEND#2 Flight Test,” 55th AIAA Aerospace Sciences Meeting, AIAA SciTech Forum, AIAA 2017-0278, 2017.

[22] Lin, J.C., Howard, F.G., and Selby, G.V., “Small Submerged Vortex Generators for Turbulent Flow Separation Control,” *Journal of Spacecraft and Rockets*, Vol. 27, No. 5 (1990), pp. 503-507.

- [23] Cockburn, B., and Shu, C.W., “The Runge–Kutta Discontinuous Galerkin Method for Conservation Laws V: Multidimensional Systems,” *Journal of Computational Physics*, Vol. 141 (1998), pp.199–224.
- [24] Huynh, H.T., “A Flux Reconstruction Approach to High-Order Schemes Including Discontinuous Galerkin Methods,” AIAA Paper 2007-4079, 2007.
- [25] Wang, Z.J., Zhang, L., and Liu, Y., “Spectral (Finite) Volume Method for Conservation Laws on Unstructured Grids IV – Extension to Two-Dimensional Systems,” *Journal of Computational Physics*, Vol. 194 (2004), pp.716-741.
- [26] Van Leer, B., “Upwind and High-Resolution Methods for Compressible Flow: From Donor Cell to Residual-Distribution Schemes,” *Communications in Computational Physics*, Vol. 1 (2006), pp.192-206.
- [27] Nishikawa, H., “A First-order System Approach for Diffusion Equation. I: Second-order Residual-Distribution Schemes” *Journal of Computational Physics*, Vol. 227 (2007), pp.315–352. doi:10.1016/j.jcp.2007.07.029
- [28] Clain, S., Diot, S., and Loubère, R.: A high-order finite volume method for systems of conservation laws— Multi-dimensional Optimal Order Detection (MOOD), *Journal of Computational Physics*, Vol.230, pp.4028–4050, 2011.
- [29] Gnoffo, P.A., “Updates to Multi-Dimensional Flux Reconstruction for Hypersonic Simulations on Tetrahedral Grids,” AIAA 2010-1271, 2010.
- [30] Stimpson, C.J., Ernst, C.D., Knupp, P., Pébay, P.P., and Thompson, D., “The Verdict Geometric Quality Library”, SANDIA REPORT, SAND2007-1751, Sandia National Laboratories, 2007.
- [31] Mavriplis, D.J., “Revisiting the Least-Squares Procedure for Gradient Reconstruction on Unstructured Meshes,” AIAA Paper 2003-3986, 2003.
- [32] Shima, E. and Kitamura, K., “Parameter-Free Simple Low-Dissipation AUSM-Family Scheme for All Speeds,” *AIAA Journal*, Vol. 49 (2011), pp.1693-1709.
- [33] Jameson, A. and Turkel, E., “Implicit Schemes and LU Decompositions,” *Mathematics of Computation*, Vol. 37 (1981), pp. 385-397.
- [34] Spalart, P.R. and Allmaras, S.R., “A One-Equation Turbulence Model for Aerodynamic Flows,” AIAA Paper 92-0439, 1992.
- [35] Rumsey, C.L., “Apparent Transition Behavior of Widely-used Turbulence Models,” *International Journal of Heat and Fluid Flow*, Vol. 28 (2007), pp. 1460-1471.
- [36] Spalart, P. R., Deck, S., Shur, M. L., Squires, K. D., Strelets, M. Kh., and Travin, A., “A New Version of Detached-Eddy Simulation, Resistant to Ambiguous Grid Densities,” *Theoretical and Computational Fluid Dynamics*, Vol. 20 (2006), pp. 181-195.
- [37] Sun, Y., Wang, Z.J. and Liu, Y., “High-Order Multidomain Spectral Difference Method for the Navier-Stokes Equations on Unstructured Hexahedral Grids,” *Communications in Computational Physics*, Vol. 2 (2009), pp. 310-333.

- [38] Taneda, S., "Experimental Investigation of the Wake behind a Sphere at Low Reynolds Numbers," *Journal of Physical Society of Japan*, Vol. 11 (1956), pp.1104-1108.
- [39] Schlichting, H. and Gersten, K., *Boundary-Layer Theory*, 8th Edition, Springer, p.14, 2000.
- [40] Kondo, K., Aono, H., Nonomura, T., Anyoji, M., Oyama, A., Liu, T., Fuji, K., and Yamamoto, M.: Analysis of Owl-like Airfoil Aerodynamics at Low Reynolds Number Flow, *Transaction of JSASS Aerospace Technology Japan.*, Vol. 12, No. ists29, pp. Tk\_35-Tk\_40, 2014.
- [41] Hishida, M., Hashimoto, A., Murakami, K., and Aoyama, T., "A new slope limiter for fast unstructured CFD solver FaSTAR," JAXA-SP-10-012, pp. 85-90, 2011 (in Japanese).
- [42] Liu, T., Kuykendoll, K., Rhew, R., and Jones, S.: Avian Wing Geometry and Kinematics, *AIAA Journal*, Vol.44 (2006), pp.954-963.
- [43] Aogaki, T., Kitamura, K., and Nonaka, S., "Computational Study of Aerodynamic Characteristics of Reusable Rocket at High-Angle-of-Attack," AIAA 2017-1212, 55th AIAA Aerospace Sciences Meeting (AIAA SciTech 2017), Grapevine, TX, 2017.
- [44] Inatomi, A., Kitamura, K., and Nonaka, S., "Numerical Analysis on Reusable Rocket Aerodynamics with Reduced-Yaw-Force Configurations," 2017-o-3-03, 31st International Symposium on Space Technology and Science (ISTS), Matsuyama, Japan, 2017.
- [45] Weiss, J.M. and Smith, W.A.: Preconditioning Applied to Variable and Constant Density Flows, *AIAA Journal*, Vol. 33, pp. 2050-2057, 1995.
- [46] Kitamura, K., Shima, E., Fujimoto, K., and Wang, Z.J., "Performance of Low-Dissipation Euler Fluxes with Preconditioned LU-SGS at Low Speeds," *Communications in Computational Physics.*, Vol.10 (2011), pp.90-119.
- [47] Ericsson, L. E. and Reding, J. P., "Steady and Unsteady Vortex-Induced Asymmetric Loads on Slender Vehicles," *Journal of Spacecraft and Rockets*, Vol. 18 (1981), pp. 97-109.
- [48] Kumar, P. and Prasad, J. K., "Mechanism of Side Force Generation and Its Alleviation over a Slender Body," *Journal of Spacecraft and Rockets*, Vol. 53, No. 1 (2016), pp. 195-208.
- [49] Waldmann, A., Gansel, P.P., Lutz, T., and Krämer, E., "Unsteady Wake Flow Analysis of an Aircraft under low-speed Stall Conditions using DES and PIV", AIAA 2015-1096, 2015.
- [50] Jiang, G.-S. and Shu, C.-W., "Efficient implementation of weighted ENO schemes," *Journal of Computational Physics*, Vol.126 (1996), pp.202-228.
- [51] Kitamura, K. and Shima, E.: Towards shock-stable and accurate hypersonic heating computations: A new pressure flux for AUSM-family schemes, *Journal of Computational Physics*, Vol.245 (2013), pp.62-83.
- [52] Dumbser, M., Zanotti, O., Loubère, R., and Diot, S., "A posteriori subcell limiting for Discontinuous Galerkin Finite

Element method for hyperbolic system of conservation laws,” *Journal of Computational Physics*, Vol.278 (2014), pp.47-75.

[53] Sengupta, A., Wernet, M., Roeder, J., Kelsch, R., Witkowski, A., and Jones, T., “Supersonic Testing of 0.8 m Disk Gap Band Parachutes in the Wake of a 70 deg Sphere Cone Entry Vehicle,” 20th AIAA Aerodynamic Decelerator Systems Technology Conference and Seminar, AIAA 2009-2974, Washington, 2009.

[54] Takayanagi, H., Yamada, K., Maru, Y., and Fujita, K., “Development of supersonic parachute for Mars EDL demonstrator,” JSASS-2014-4168, Proceedings of 58th Space Sciences and Technology Conference, 2014 (in Japanese).

[55] Takabayashi, K., Fukumoto, K., and Kitamura, K., “Computational Study on Rigid Disk-Gap-Band Supersonic Parachute Aerodynamics,” Paper No. SBM000188, 31st International Symposium on Shock Waves (ISSW31), Nagoya, Japan, 2017.

## Figures

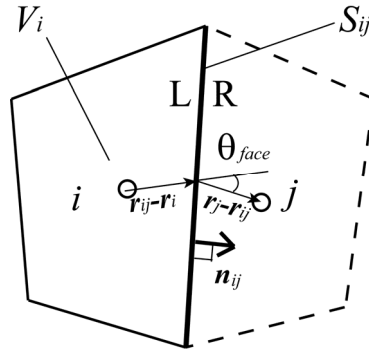


Figure 1. Schematic of cell geometric properties.

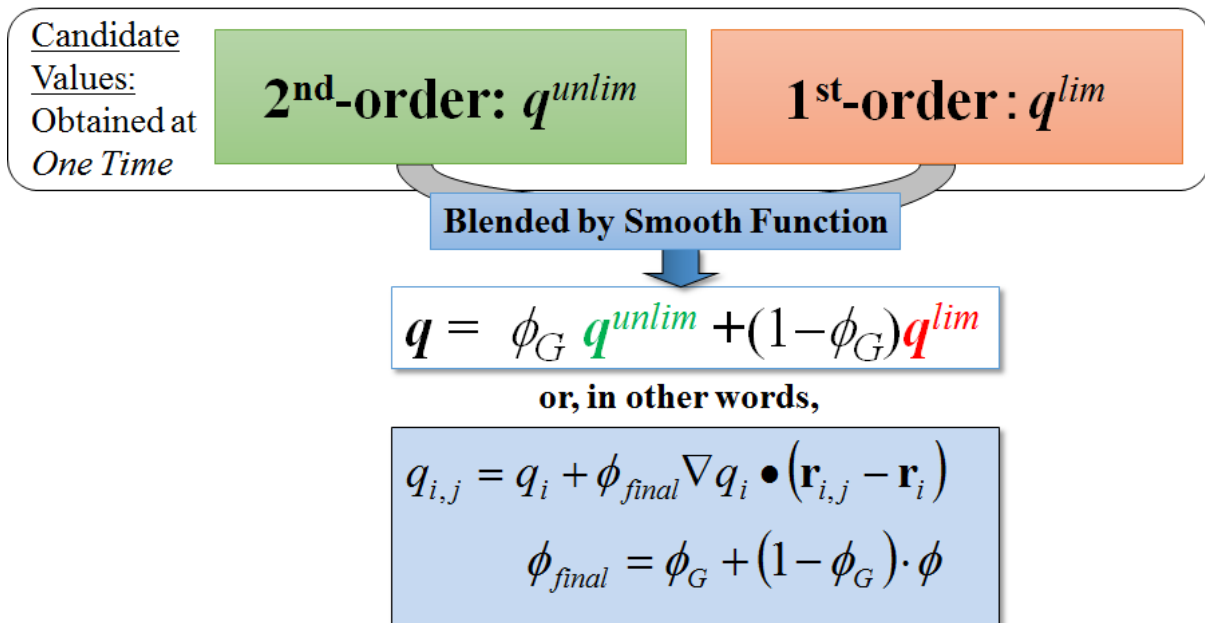


Figure 2: Core concept of Post Limiter

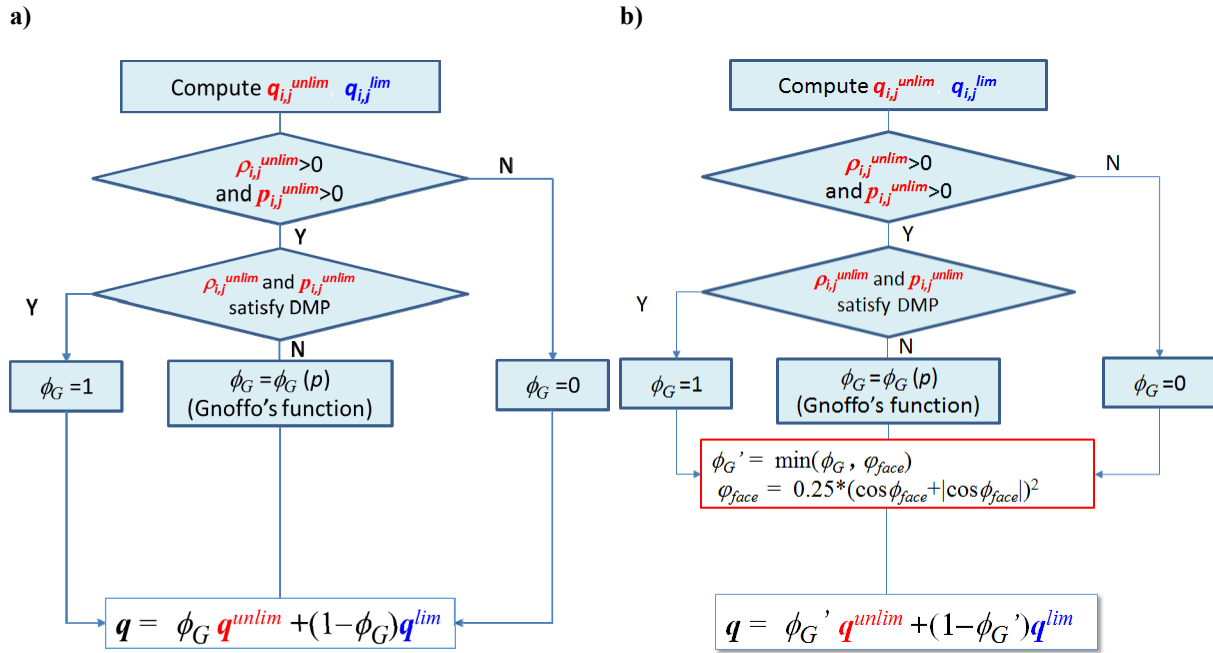


Figure 3: Flow Charts of (a) Post Limiter 1 and (b) Post Limiter 2.

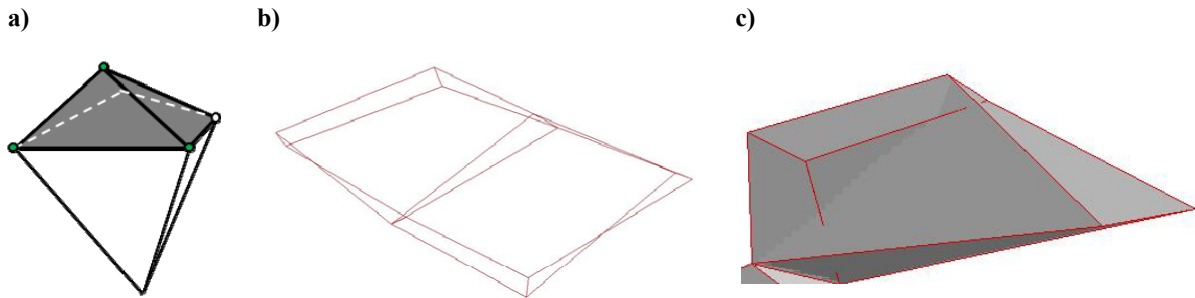


Figure 4: Examples of dirty-cell geometries (a) (gray) face composed of four points not on the same plane, (b) upper and lower surfaces flip-over and (c) edge-face interaction.

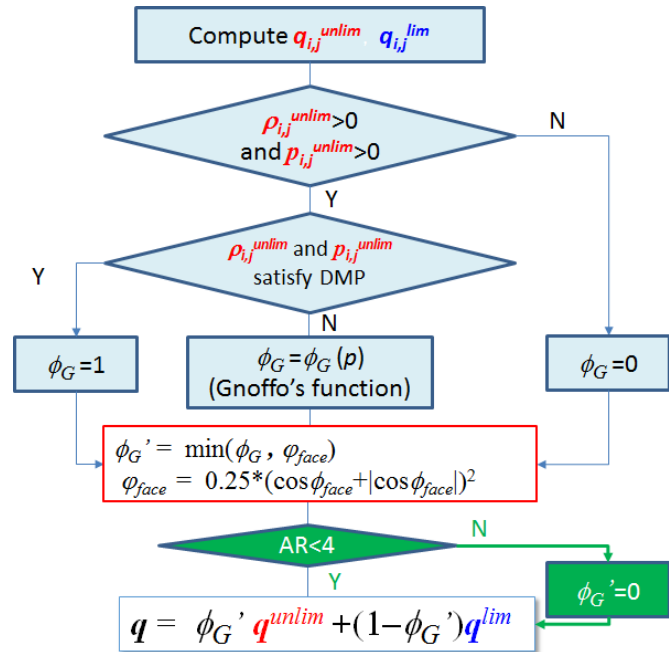


Figure 5: Flow Chart of Post Limiter 3.

a)

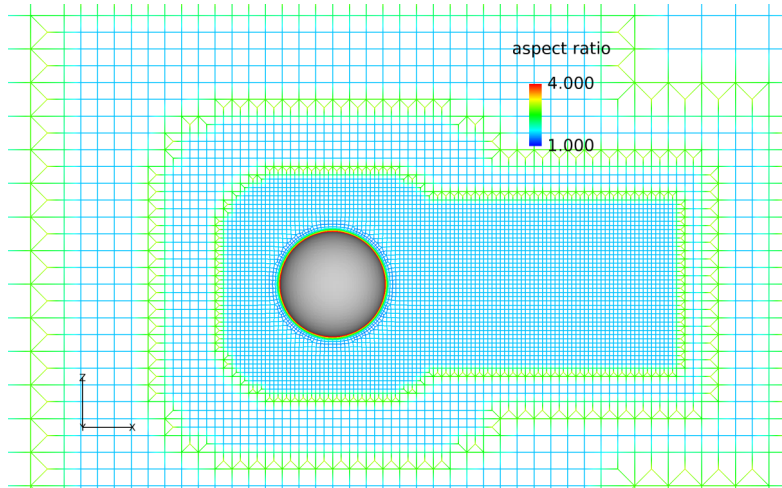
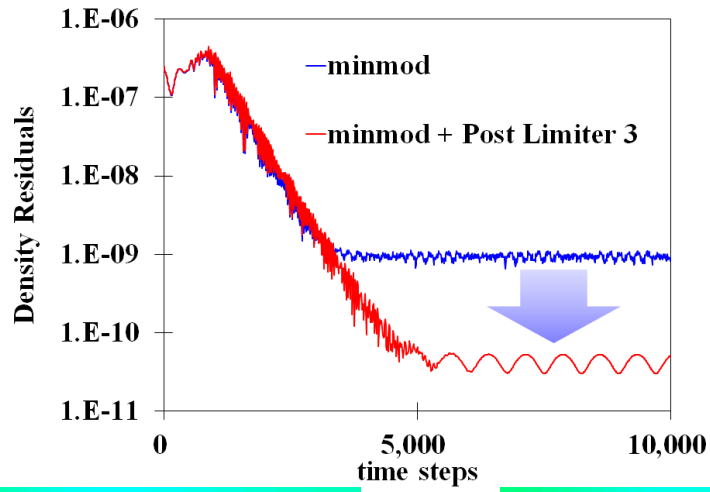
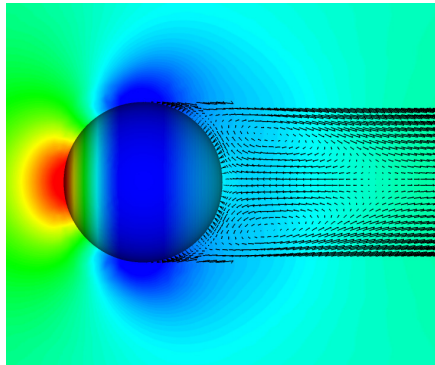


Figure 6:  $M=0.1$ ,  $Re=118$  Flow around Sphere, (a) Grid colored with  $AR$  ( $1 \leq AR \leq 4$ ), (b) Density Residual Histories, (c) Pressure and Wake Velocity (minmod-only), (d) Pressure and Wake Velocity (minmod + Post Limiter 3), and (e) Pressure differences between (c) and (d), *continued*.

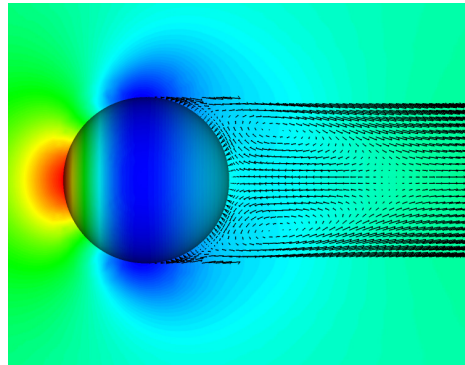
b)



c)



d)



e)

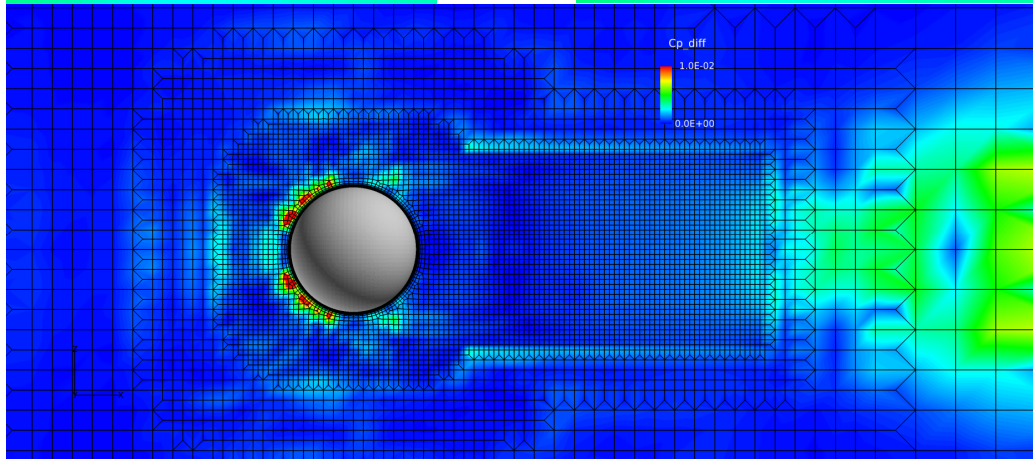


Figure 6:  $M=0.1$ ,  $Re=118$  Flow around Sphere, (a) Grid colored with  $AR$  ( $1 \leq AR \leq 4$ ), (b) Density Residual Histories, (c) Pressure and Wake Velocity (minmod-only), (d) Pressure and Wake Velocity (minmod + Post Limiter 3), and (e) Pressure differences between (c) and (d), concluded.



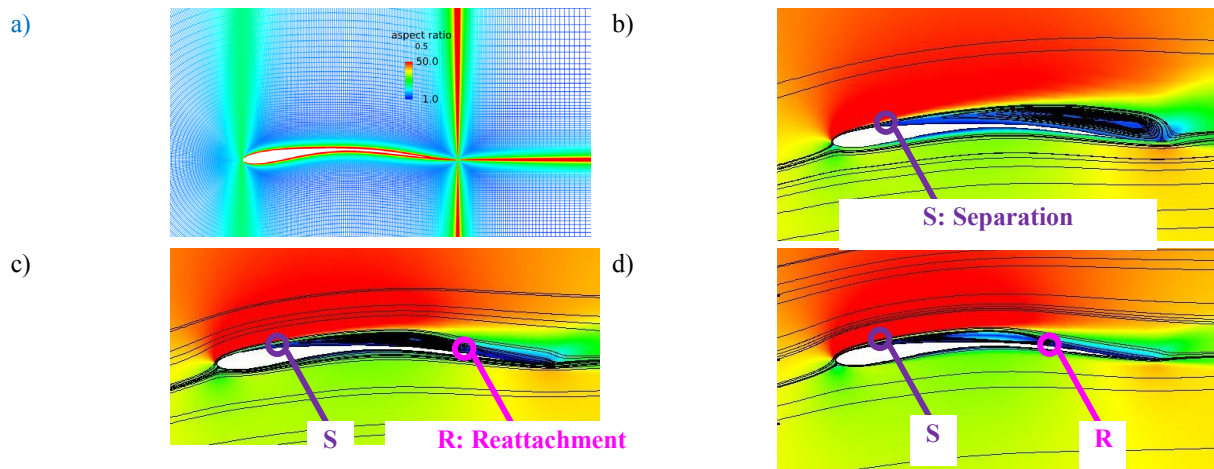
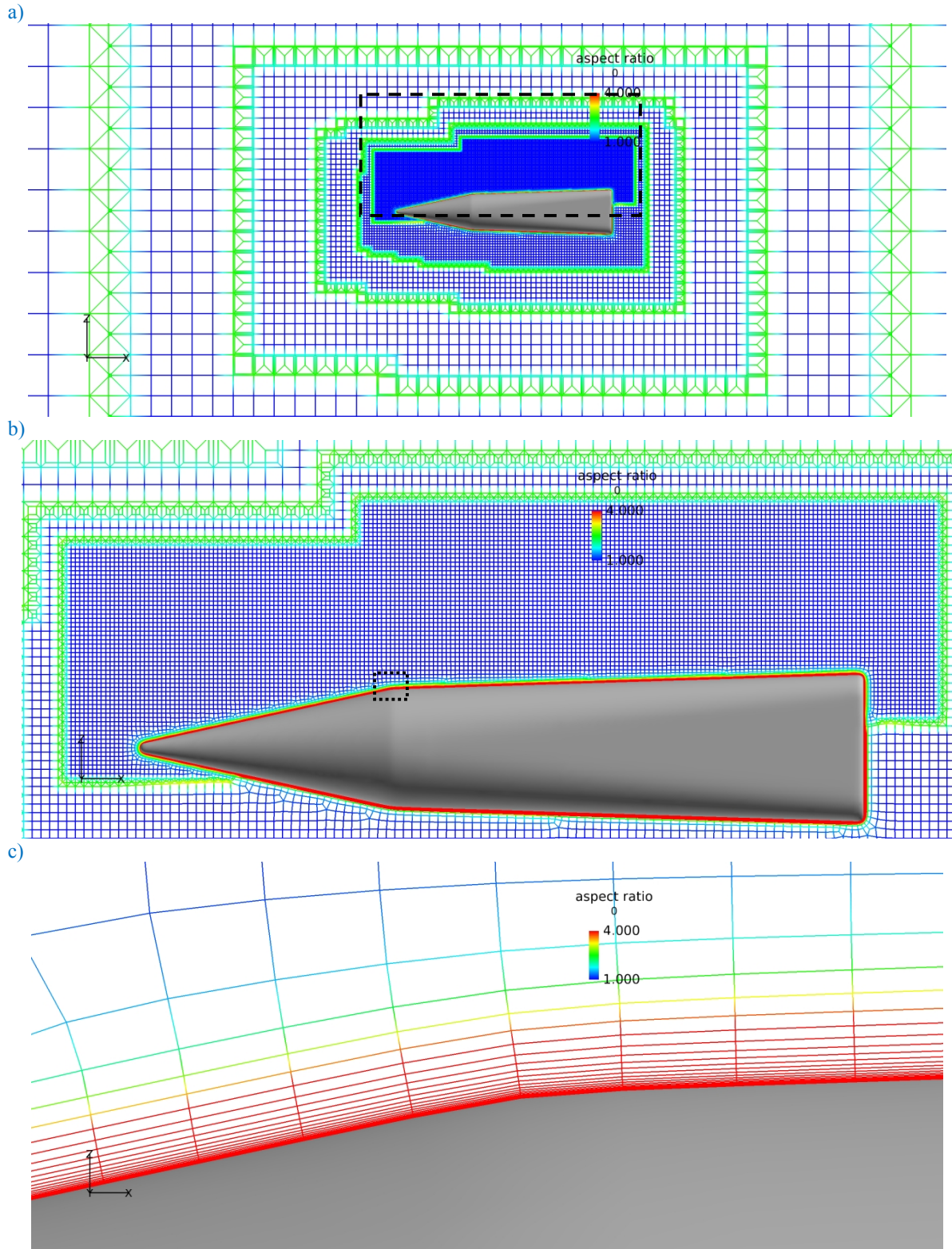
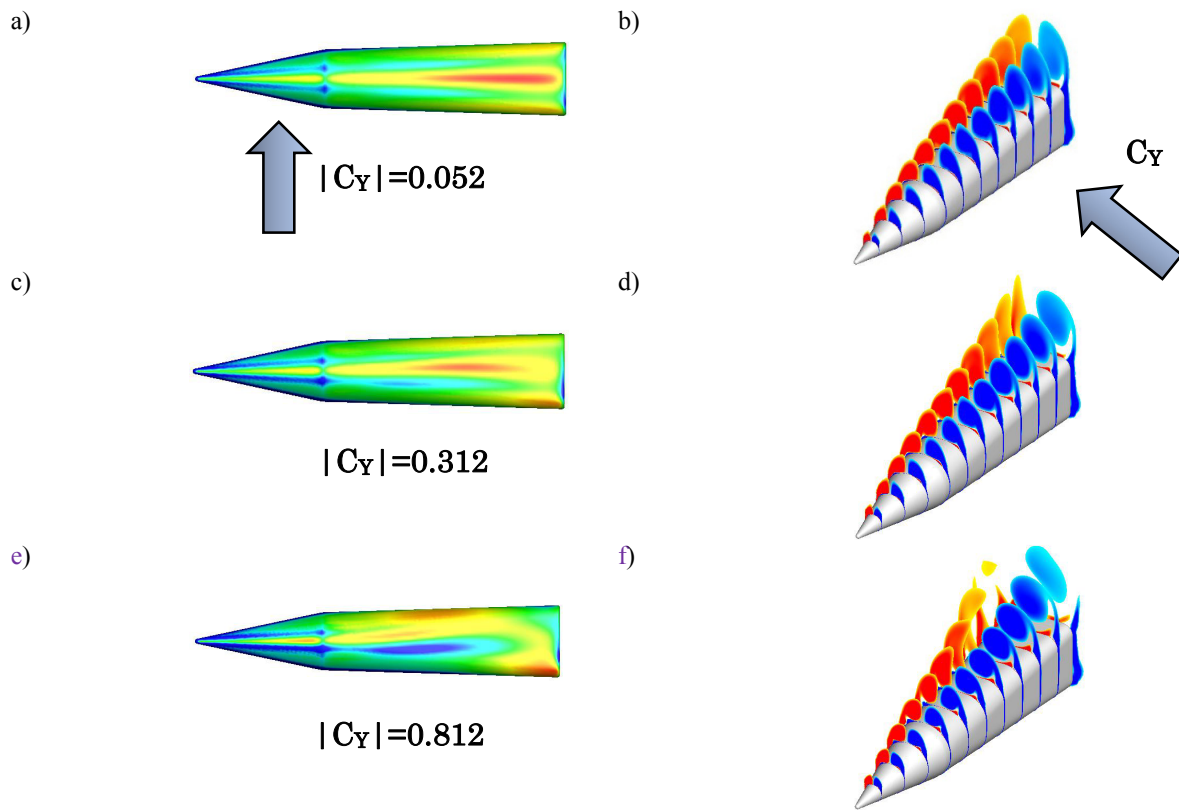


Figure 7: Owl-like airfoil ( $M=0.2$ ,  $Re=23000$ ,  $\alpha=6$  deg.), (a) Grid colored with  $AR$  ( $1 \leq AR \leq 50$ ), (b) Coarse [Hishida(vL)-only], (c) Coarse [Hishida(vL) + Post Limiter 3], (d) Baseline [Hishida(vL)-only].



**Figure 8: Computational Grid colored with  $AR$  ( $1 \leq AR \leq 4$ ) around Slender Body, (a) overview, (b) close-up view around the body, and (c) close-up view near the wall.**



**Figure 9: Computed Results of Flow around Slender Body at High Angle-of-Attack ( $M=0.08643$ ,  $Re=6 \times 10^5$ ,  $\alpha=50$  deg.) (a) minmod-only (pressure), (b) minmod-only (axial vorticity), (c) minmod + Post Limiter 3 (pressure), (d) minmod + Post Limiter 3 (axial vorticity), (e) no limiter (pressure), (f) no limiter (axial vorticity)**

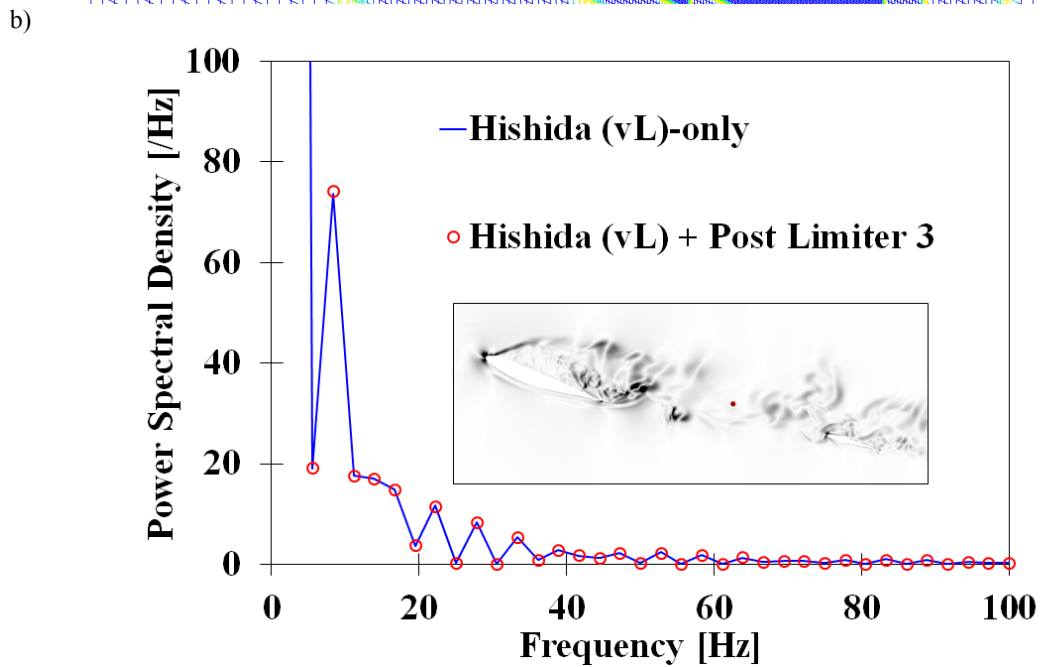
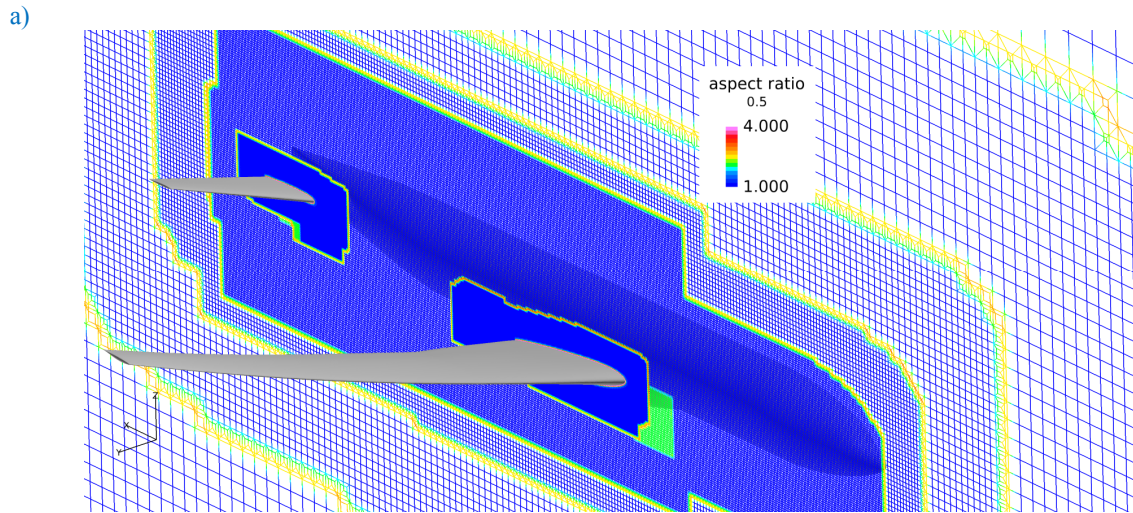
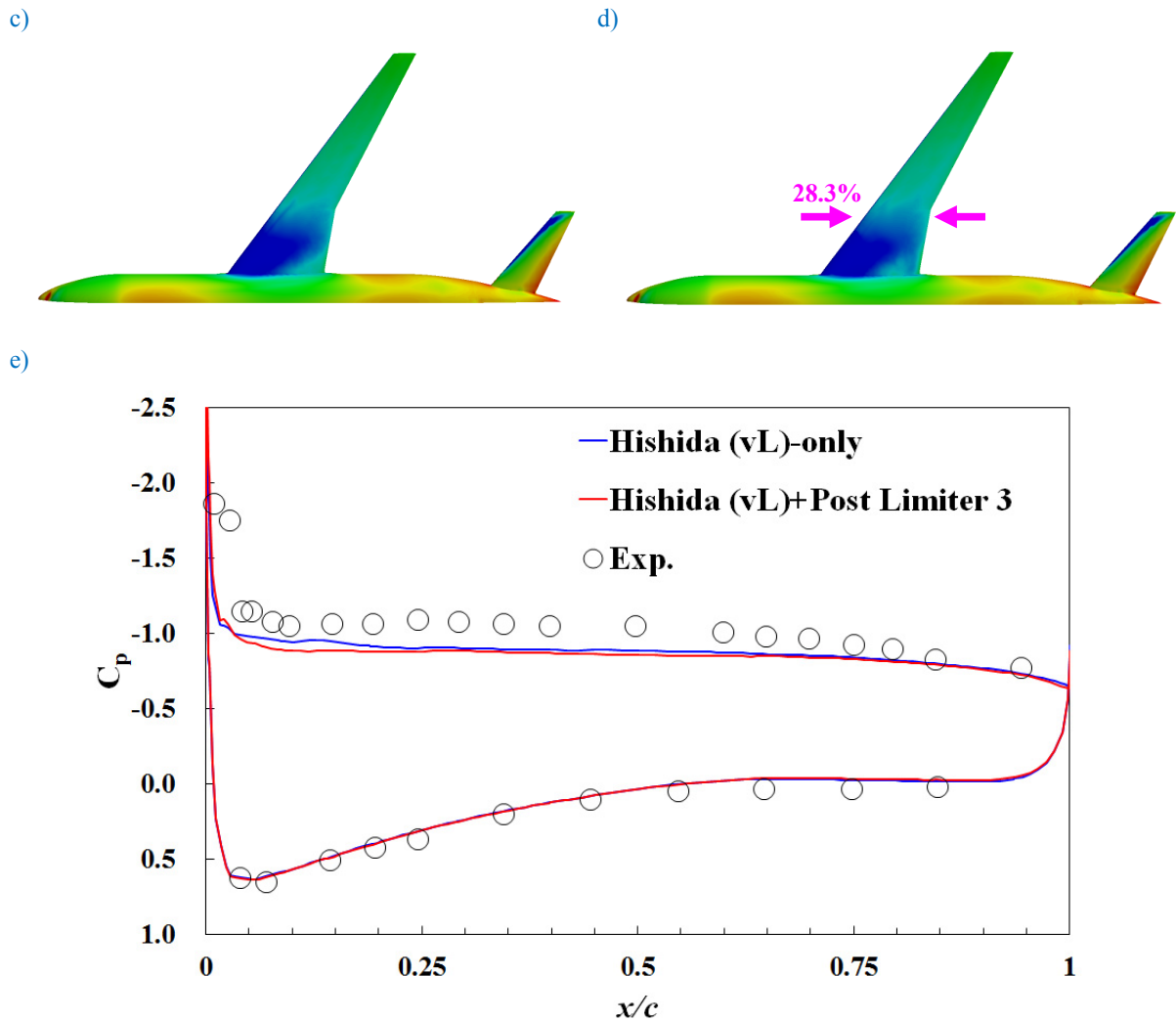
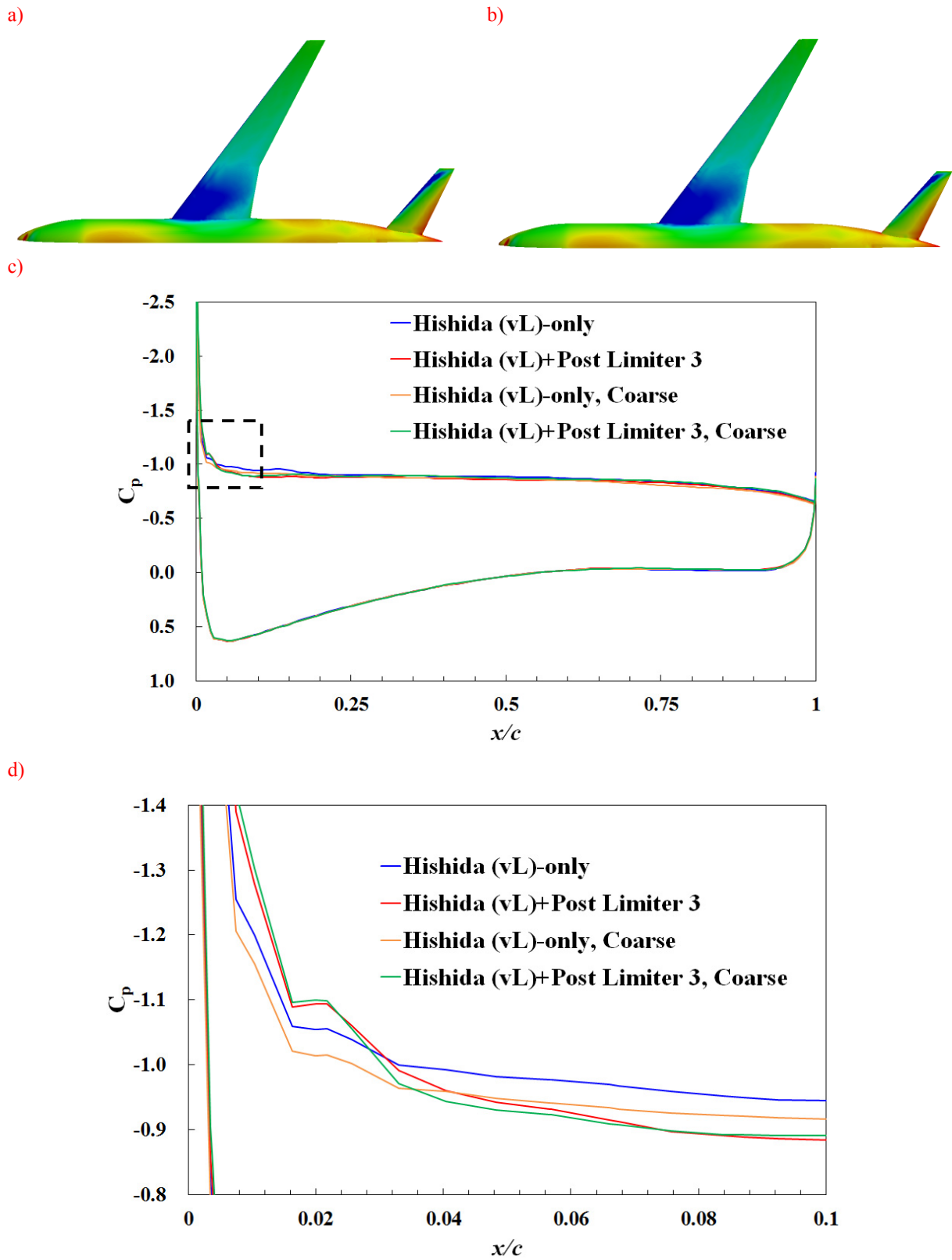


Figure 10: Three-dimensional Aircraft Flow Computation, (a) Grid colored with  $AR$  ( $1 \leq AR \leq 4$ ), (b) Power Spectral Density Profiles in the Wake of Main Wing ahead of Tail Wing (Red Point in the Superimposed Plane), (c)  $C_p$ -Profile ( $-1.0 < C_p < 0.2$ ) on Top Surface [Hishida (vL)-only], (d)  $C_p$ -Profile ( $-1.0 < C_p < 0.2$ ) on Top Surface [Hishida (vL) + Post Limiter 3], and (e)  $C_p$ -Profiles at 28.3% Spanwise Cross-Section of Main Wing (Compared with Experimental Data [49]), continued.



**Figure 10: Three-dimensional Aircraft Flow Computation, (a) Grid colored with  $AR$  ( $1 \leq AR \leq 4$ ), (b) Power Spectral Density Profiles in the Wake of Main Wing ahead of Tail Wing (Red Point in the Superimposed Plane), (c)  $C_p$ -Profile ( $-1.0 < C_p < 0.2$ ) on Top Surface [Hishida (vL)-only], (d)  $C_p$ -Profile ( $-1.0 < C_p < 0.2$ ) on Top Surface [Hishida (vL) + Post Limiter 3], and (e)  $C_p$ -Profiles at 28.3% Spanwise Cross-Section of Main Wing (Compared with Experimental Data [49]), concluded.**



**Figure 11: Three-dimensional Aircraft Flow Computation (Coarse grid), (a)  $C_p$ -Profile ( $-1.0 < C_p < 0.2$ ) on Top Surface [Hishida (vL)-only], (b)  $C_p$ -Profile ( $-1.0 < C_p < 0.2$ ) on Top Surface [Hishida (vL) + Post Limiter 3], (c)  $C_p$ -Profiles at 28.3% Spanwise Cross-Section of Main Wing, and (d) close-up view of (c).**

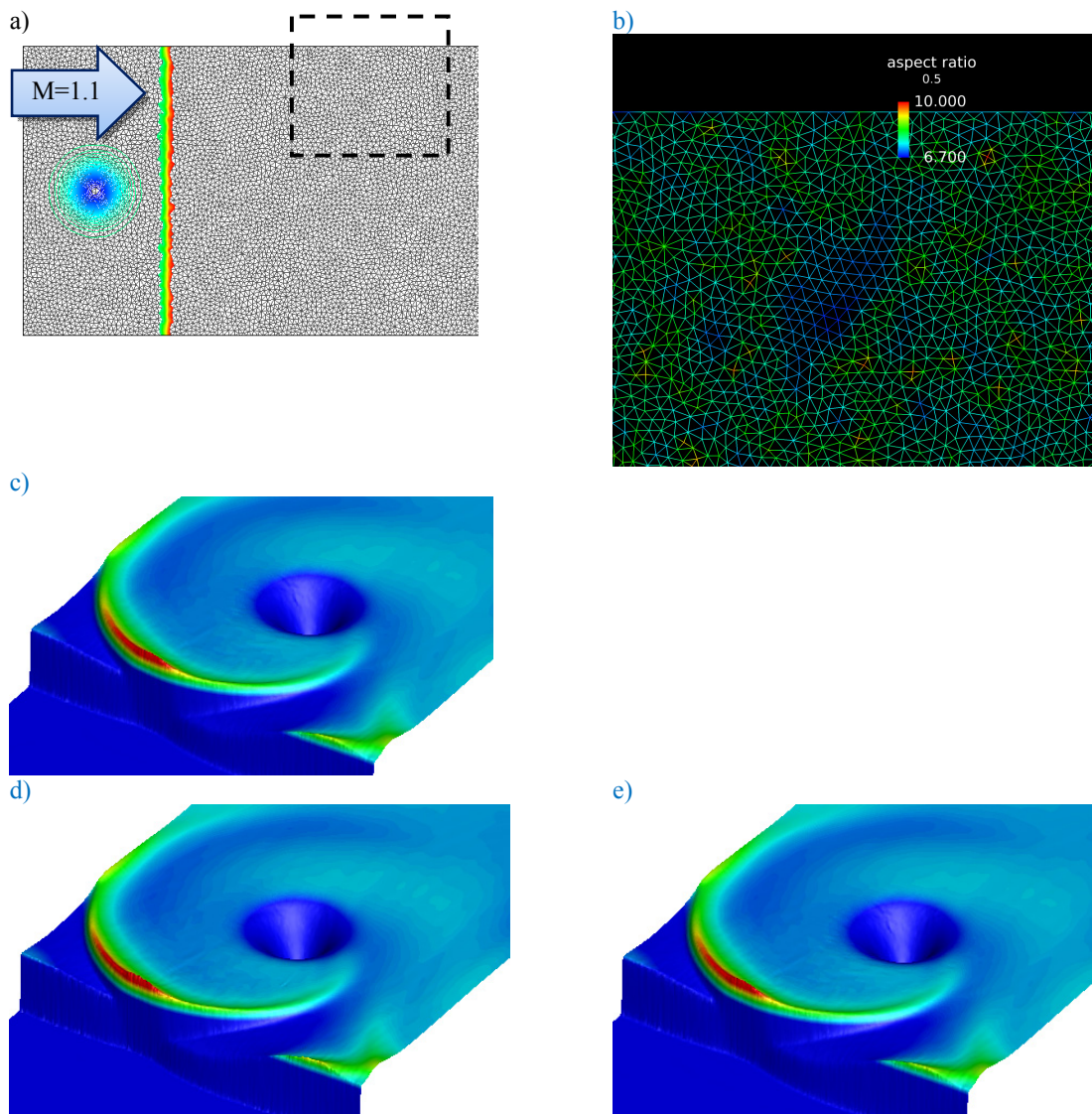
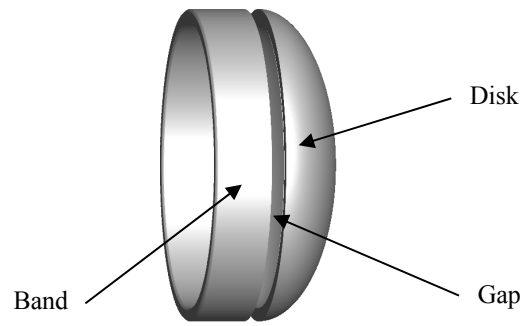


Figure A.1: Shock/Vortex Interaction ( $M=1.1$ , Inviscid) (a) Grid and Initial Conditions, (b) Grid colored with  $AR$  ( $6.6 \leq AR \leq 10.2$ ), (c) minmod-only, (d) minmod + Post Limiter 2, (e) minmod + Post Limiter 3.



**Figure B.1: Supersonic Parachute.**



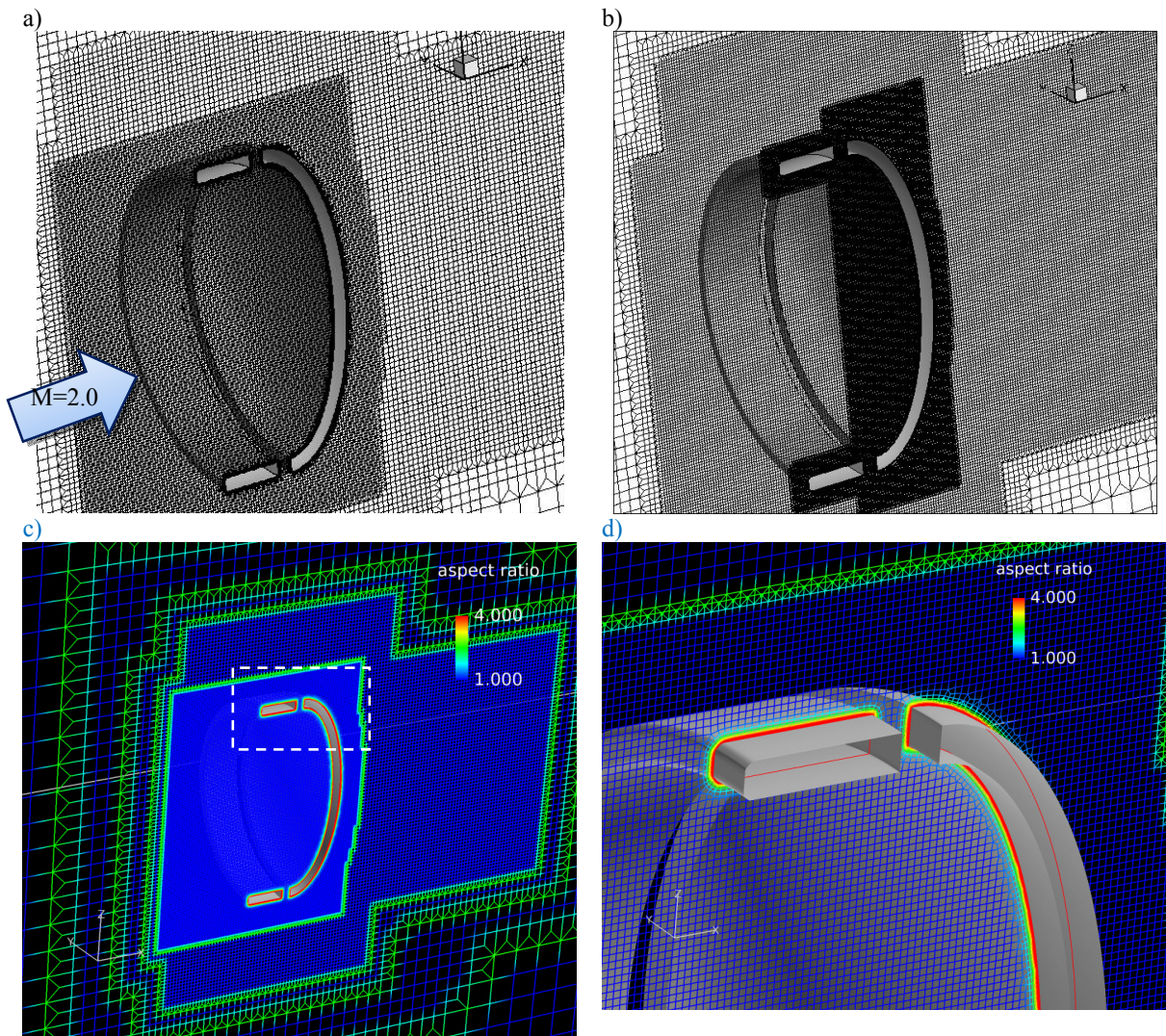
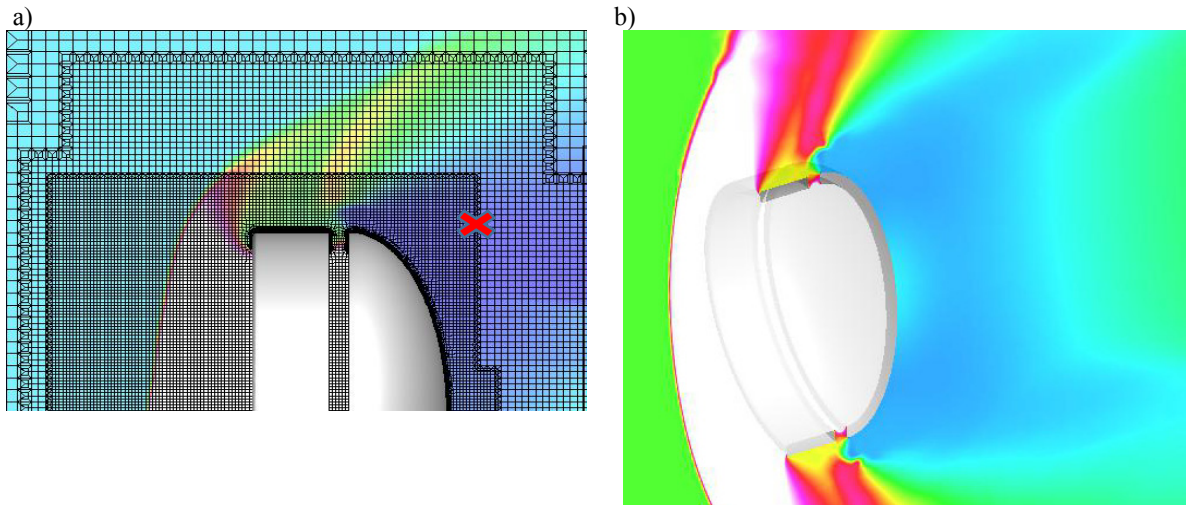
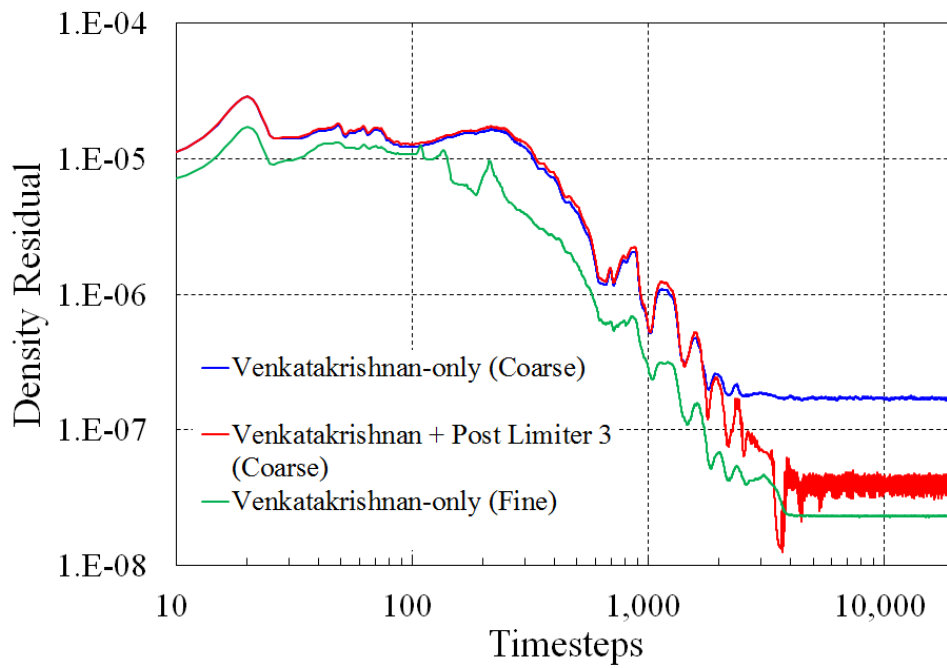


Figure B.2: Computational Grids for Supersonic Parachute ( $M=2.0$ ,  $Re=2 \times 10^6$ ) (a) Coarse (2.8M cells), (b) Fine (10.5M cells), (c) Coarse colored with  $AR$  ( $1 \leq AR \leq 4$ ), (d) Band vicinity close-up of (c).



**Figure B.3: Computational Results for Supersonic Parachute ( $M=2.0$ ,  $Re=2 \times 10^6$ ) (a) Post Limiter 2 (Coarse, right before divergence at red cross), (b) Post Limiter 3 (Coarse)**



**Figure B.4: Density Residual Histories of Supersonic Parachute ( $M=2.0$ ,  $Re=2 \times 10^6$ )**

## Tables

Table 1 Typical  $AR$  Values for Typical Cell Configurations ( $L$ : Edge Length of Bottom Surface)

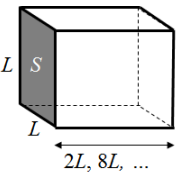
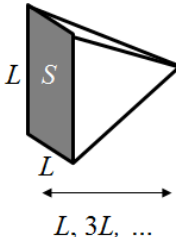
Cell	$S$ (Bottom Surface Area)	Height	$V$ (Volume)	$AR$
Cube	$L^2$	$L$	$L^3$	1.00
Rectangular 	$L^2$	$2L$	$2L^3$	1.59
		$8L$	$8L^3$	4.00
Pyramid 	$L^2$	$L$	$L^3/3$	2.08
		$3L$	$L^3$	1.00
		$9L$	$3L^3$	2.08
		$27L$	$9L^3$	4.33
Tetrahedron	$(\sqrt{3}/2)L^2$	$3L$	$(\sqrt{3}/2)L^3$	1.05
Prism	$(\sqrt{3}/2)L^2$	$L$	$(\sqrt{3}/2)L^3$	1.05

Table 2 Summary of Post Limiters 1 through 3

Versions	Primary Target Grids	Descriptions	Comments
Post Limiter 1	1D or 2D Structured	Fig. 3a	-
Post Limiter 2	2D Unstructured	Fig. 3b, Eq. (3)	Post Limiter 1 + “cell orientation-angle” $\theta_{face}$ (Fig. 1)
Post Limiter 3	3D Unstructured	Fig. 5, Eqs. (3)(4)	Post Limiter 2 + “aspect-ratio-like number” $AR$ (Eq. (4)) for dirty-cell treatment

Table 3 Summary of Three-Dimensional Aircraft Flow Computations

Slope Limiter	Post Limiter	Computations
Without limiter	-	Diverged
Hishida (vL)	Without Post Limiter	Successful
Hishida (vL)	Post Limiter 1	Diverged
Hishida (vL)	Post Limiter 2	Diverged
Hishida (vL)	Post Limiter 3	Successful